Journal of Materials Science & Technology 53 (2020) 192–199

Contents lists available at ScienceDirect

Journal of Materials Science & Technology

journal homepage: www.jmst.org

Research Article

High-throughput investigations of configurational-transformation-dominated serrations in CuZr/Cu nanolaminates

William Yi Wang[a,1], Bin Gan[a,b,c,1], Deye Lin[d], Jun Wang[a], Yiguang Wang[a], Bin Tang[a], Hongchao Kou[a], Shunli Shang[e], Yi Wang[e], Xingyu Gao[d], Haifeng Song[d], Xidong Hui[f], Laszlo J. Kecskes[g], Zhenhai Xia[a], Karin A. Dahmen[h], Peter K. Liaw[i], Jinshan Li[a,*], Zi-Kui Liu[e]

[a] State Key Laboratory of Solidification Processing, Northwestern Polytechnical University, Xi'an, 710072, China
[b] Beijing Key Laboratory of Advanced High Temperature Materials, Central Iron and Steel Research Institute, Beijing, 100081, China
[c] IMDEA Materials Institute, Calle Eric Kandel 2, Getafe, Madrid, 28906, Spain
[d] CAEP Software Center for High Performance Numerical Simulation, Institute of Applied Physics and Computational Mathematics, Beijing, 100088, China
[e] Department of Materials Science and Engineering, The Pennsylvania State University, University Park, PA, 16802, USA
[f] State Key Laboratory for Advanced Metals and Materials, University of Science and Technology Beijing, Beijing, 100083, China
[g] Hopkins Extreme Materials Institute, Johns Hopkins University, Baltimore, MD, 21218, USA
[h] Department of Physics, University of Illinois at Urbana Champaign, Urbana, IL, 61801, USA
[i] Department of Materials Science and Engineering, The University of Tennessee, Knoxville, TN, 37996, USA

ARTICLE INFO

Article history:
Received 28 December 2019
Received in revised form 12 February 2020
Accepted 20 February 2020
Available online 6 May 2020

Keywords:
Nanolaminates
Serration
Configurational transformation
Molecular dynamics
Metallic glass

ABSTRACT

Metallic amorphous/crystalline (A/C) nanolaminates exhibit excellent ductility while retaining their high strength. However, the underlying physical mechanisms and the resultant structural changes during plastic deformation still remain unclear. In the present work, the structure-property relationship of CuZr/Cu A/C nanolaminates is established through integrated high-throughput micro-compression tests and molecular dynamics simulations together with high-resolution transmission electron microcopy. The serrated flow of nanolaminates results from the formation of hexagonal-close-packed (HCP)-type stacking faults and twins inside the face-centered-cubic (FCC) Cu nano-grains, the body-centered-cubic (BCC)-type ordering at their grain boundaries, and the crystallization of the amorphous CuZr layers. The serration behavior of CuZr/Cu A/C nanolaminates is determined by several factors, including the formation of dense dislocation networks from the multiplication of initial dislocations that formed after yielding, weak-spots-related configurational-transitions and shear-transition-zone activities, and deformation-induced devitrification. The present work provides an insight into the heterogeneous deformation mechanism of A/C nanolaminates at the atomic scale, and mechanistic base for the microstructural design of self-toughening metallic-glass (MG)-based composites and A/C nanolaminates.

1. Introduction

In recent few decades, metallic glasses (MGs) and nanolaminates have attracted considerable attention due to their high strength and hardness [1–3]. Serration, a saw-tooth-like variation of the stress in the plastic regime of stress-strain curves, is an important and ubiquitous deformation behavior in structural and functional materials, including MGs, high-entropy alloys, superalloys, ordered intermetallics, shape-memory alloys, carbon steels, twin-induced plasticity (TWIP) steels, Al-Mg alloys, nanomaterials, and magnetic functional materials, etc [1–6]. This jerky flow has been long associated with the underlying fundamental deformation behavior of materials, such as dynamic strain aging or the competition between diffusing solutes pinning dislocations and the dislocations breaking free of this blockage. Therefore, a careful study of serrations would provide a deeper understanding of strengthening and toughening mechanisms and the accompanying structural evolution during plastic deformation, from which new strategies could be made for the design of more viable candidate

* Corresponding author.
E-mail address: ljsh@nwpu.edu.cn (J. Li).
[1] These authors contribute equally to this work.

https://doi.org/10.1016/j.jmst.2020.04.024
1005-0302/

materials for critical applications. For example, weak spots in MGs, or clusters of atoms, which strongly participate in soft vibrational modes, are typically loosely-packed "geometrically unfavored motifs (GUM)" [2,3,7,8], restrain the shear-band nucleation and propagation, thereby rejuvenating the amorphous structure into a more deformable state, and thus adjusting the overall alloy composition to be enriched with greater structural heterogeneity [7]. The nucleation of shear bands (SBs) prefers to occur at weak sites/spots [9], which most likely serve as fertile sites for inelastic shear transformations and result in the formation of both structural and mechanical heterogeneities [7]. It is also known that nanocrystallites could form in MGs during nanoindentation, severe bending, or high-energy ball milling, which is referred to as deformation-induced devitrification (DID) [9,10]. Furthermore, in Cu-Zr MGs, it has been shown that the excess free volume combined with smaller shear-transformation-zones (STZs) could trigger strain-softening behavior [11]. The transformation-mediated ductility in CuZr-based bulk metallic glasses (BMGs) has been captured, in which the nanocrystallines precipitate polymorphically and subsequently undergo twinning, enhancing the ductility of BMGs [12]. The concept of the DID-mediated superior deformability via an externally-supplied, dislocation-stimulated-STZs would support a new and universally-applicable strategy to synthesize self-toughening bulk MGs and MG matrix composites [13].

MGs usually undergo the inhomogeneous deformation through shear banding, leading to their low ductility/toughness, which is due to the lack of dislocation-mediated crystallographic slip compared to those present in crystalline materials. As a result, it has been a major challenge to *a priori* identify the effect of structural defects that cause atomic rearrangements to occur under externally-applied stresses [2,8,14–16]. Thus, to alleviate the detrimental effects of shear banding and ensure a more widespread and safe use of BMG materials, there is a renewed global interest in incorporating intrinsically-formed or extrinsically-added crystalline or quasi-crystalline phases into the BMG matrix to arrest and deflect the propagation path of shear bands [2,8,14,15,17,18]. Recent studies have shown that the incorporation of crystalline phases into MGs can effectively enhance their ductility while retaining their high strength, as observed in the amorphous/crystalline nanolaminates (A/C NLs) and MG-based composites [11,12,18–21]. For instance, it is the B2 CuZr nanocrystals, with a critical softening of the instantaneous shear modulus in $(Cu_{0.5}Zr_{0.5})_{100-x}Al_x$ MGs, which are considered to be the origin for subsequent twinning, retarding the nascent formation of shear bands and cracks [12]. They can hinder the propagation of primary shear bands and promote the formation and multiplication of shear bands. The volume fraction, composition and morphological shape, and distribution of such microstructural features are important and key parameters for plastically shielding of an opening crack tip to limit the continuation and extension of shear bands. In turn, this trend will result in the enhanced plasticity, increased strengths as well as a change of deformation and fracture mechanisms. With extrinsically-added crystalline phases, for example, multilayers consisting of alternating MG and nanocrystalline phases are revealed to be manufactured in a relative easy fashion and could be produced via various thin-film fabrication processes, such as vapor deposition and sputter deposition. As for the nanolaminates, the crystalline layers appear to enhance the mechanical performance of the brittle MG layers. It is the unique motion of the active dislocations in the nanocrystalline layers that mainly contributes to the attainment of the improved behavior via an additive co-deformation process. Thus, the development of nano-composites is primarily aimed to improve the room-temperature toughness and develop laminated composites with superplasticity. This analogy suggests that the A/C multilayers can be constructed in such a way that the crystalline phase is rigidly attached to the amorphous phase. As such, it can absorb the kinetic energy carried by the shear bands, which initiate in the amorphous phase. As they impinge and are arrested at the interface, larger global plasticity in the amorphous phase thus becomes possible.

As for A/C NLs, the layers containing nanocrystalline grains have two functions: one is to produce the unique inelastic shear (slip or twinning) transfer at the amorphous/nano-crystal (A/nC) interface; and, the other is to suppress local-stress concentrations due to the paucity of dislocation pileups and operating twinning systems [22]. Micropillar compression tests prove to be a suitable method to study the deformation behavior of nanolaminate composites. Previously, CuZr/Cu A/nC NLs micropillars have displayed a large deformability of <20 % and, simultaneously, high strengths of <1.5 GPa under uniaxial compression [20]. The advantage of the nanolaminate structures is that their interfaces are stationary and can be easily located after the deformation, leading to a convenient way for quantitatively analyzing the deformation mechanics and as-deformed microstructures [23]. However, the underlying physical mechanisms for the structural evolution and mechanically-heterogeneous behavior of MG composites and A/nC NLs alike, such as the appearance of the serrated flow, still remain unclear [13,24].

The goal of the present work is to uncover the mechanisms at the atomic and electronic scales for the structural/configurational and dynamic heterogeneities of a $Cu_{50}Zr_{50}$/Cu A/nC NLs during plastic deformation. Integrated high-throughput micro-compression measurements and a molecular-dynamic study were carried out to determine the effects of local atomic arrangements, including short-range ordering, weak spots in the amorphous CuZr, and grain boundaries in the nanocrystalline Cu, on the configurational transformation that dominates serrations. The type-C serration behavior [1] of the CuZr/Cu A/nC NLs was correlated with the shear-bands patterns and the nanoscale structural heterogeneity, both of which are dominated by changes in the local microstates/configurations. It was found that the presence of a ductile nanocrystalline phase in the nanolaminates could slow down the speed of shear-band propagation and prevent catastrophic shear banding. The underlying mechanism of the serrated flow of nanolaminates was considered as the results of the hexagonal-close-packed (HCP)-type stacking faults and twining inside the face-centered-cubic (FCC) Cu nano grains, the body-centered-cubic (BCC)-type ordering at their grain boundaries, and the short-to-middle range orders in the amorphous CuZr.

2. Experimental

2.1. Materials and structural characterizations

The amorphous CuZr/nc Cu nanolaminates were deposited on Si(100) wafers by direct current magnetron sputtering. Targets of pure Cu (99.99 at.%) and Zr (99.99 at.%), each with 5.08 cm in diameter, were used to deposit alternating layers of the amorphous CuZr layer and the pure nc Cu layers. The base pressure was $<10^{-7}$ mbar, and the processing pressure was 3×10^{-3} mbar using the pure Ar gas. The substrate rotated at a frequency of 10 min^{-1}. The thicknesses of CuZr (amorphous) and Cu (nanocrystalline) is 100 nm and 10 nm, respectively. The total stacked thickness of the CuZr/Cu nanolaminates is 1200 nm with an amorphous CuZr cap layer. The structure of the as-deposited thin films was characterized by the X-ray diffraction (XRD, Bruker D8 diffractometer) with a CuK_α radiation, field-emission scanning electron microscopy (SEM, FEI Helios Nanolab 600i), and transmission electron microscopy (TEM, JEOL JEM-2200FS).

2.2. Micro-compression measurements

To explore the strain-rate dependence and serrated flow behavior of CuZr/Cu multilayers, pillars with initial diameters of 630 nm

were fabricated, using a dual-beam focused ion beam (FIB) system (FEI Helios Nanolab 600i) operated at a final beam current of 86 pA and a constant accelerating voltage of 30 kV. The pillars were inside a 25 μm diameter crater, leaving enough space for the 10 μm-diameter diamond flat punch to avoid the simultaneous contact with the surrounding bulk and the pillar. The Hysitron TI 950 instrumented indentation platform was equipped with a flat diamond punch. Prior to the testing of the nanolaminates, the instrument was well calibrated with the fused silica to acquire the system compliance. The loads and displacements were simultaneously recorded at a frequency of 30 kHz. The high acquisition rate of the instrument allowed us to quantify the propagation speed of the shear band. After reaching the preset maximum displacement, a 10 s holding segment followed. Unloading was done at the same rate as the loading. The morphology of the pillars after deformation was further examined by SEM. To gain further insight into the strain-rate sensitivity of the micropillars and identify the reason for the increased viscosity of the shear bands, the site-specific TEM lamellas containing the deformed pillars were prepared by an *in-situ* lift-out method and FIB milling. A 200 kV JEOL JEM-2200FS TEM was used for high-resolution TEM imaging.

2.3. Molecular dynamics (MD) simulations

The $Cu_{50}Zr_{50}$/Cu nanolaminates were prepared in three steps. Firstly, a randomly-alloyed $Cu_{50}Zr_{50}$ sample consists of 32,000 atoms within the FCC lattice structure was created. The initial box size was set according to the FCC-Cu's experimental lattice parameter. It was firstly annealed at 2500 K for 100 ps under the constant number of atoms, pressure and temperature (NPT) ensemble to obtain a fully-relaxed liquid alloy, and then was quenched from 2500 K to 50 K at a constant cooling rate of 1×10^8 K/s to produce $Cu_{50}Zr_{50}$ MG samples. Secondly, the polycrystalline Cu sample was created with the help of the ATOMSK code [25]. In a box with 200 Å × 200 Å × 200 Å, 8 FCC-Cu grains were generated randomly with different crystallographic orientations using the Voronoi tessellation method [25]. The overlapping atoms (with the nearest neighbor distances within 1.5 Angstroms) near the grain boundaries were deleted. Then, this sample was equilibrated at 50 K for 100 ps under the NPT ensemble. Finally, the nanolaminates were constructed by concatenating the polycrystalline Cu layers and MG layers together. To eliminate the interface misfit, we replicated the MG sample with a proper size, and cut it to make both the numbers of atoms and sizes of the Cu layers and the MG layers match and be comparable. Accordingly, as shown in the Fig. S4 in the Supplementary Information, the schematic diagram presents the procedure constructing the supercell of $Cu_{50}Zr_{50}$/Cu A/C NLs based on the individual amorphous $Cu_{50}Zr_{50}$ and polycrystalline Cu supercells. The total number of atoms in the nanolaminate sample is about 2 million. The $Cu_{50}Zr_{50}$/Cu NL was also equilibrated at 50 K for 100 ps under the NPT ensemble.

Below, the compression simulation of the nanolaminate was conducted at a constant engineering strain rate of 1×10^8 s^{-1}. We applied the loading along the *z*-axis; the *x* and *y* axes were allowed to be adjusted on-the-fly during the simulation. The external pressure was set to zero, and the temperature was controlled using the Nóse-Hoover thermostat method [26,27] at 50 K.

All the molecular dynamics (MD) simulations were performed, using the LAMMPS code [28], and the periodic boundary conditions were applied to all three dimensions. The equation of motion was solved, using a velocity-Verlet integrator with a time step of 1 fs. The embedded-atom-method (EAM) potential developed by Mendelev et al. (CuZr-2#) [29] was used to describe the interatomic interactions of the $Cu_{50}Zr_{50}$/Cu system. The visualizations and analyses of the atomic data were carried out with the help of the OVITO code and its Python API developed by Stukowski [30]. The Von-Mises atomic local shear strain [31] and adaptive Common Neighbor Analysis (CNA) methods [30] were used to track the microstructure evolution in the nanolaminates subjected to deformation. The stress was calculated by the *zz* component of the virial stress.

3. Results and discussion

3.1. Microstructure and micro-compression of the CuZr/nc Cu A/C nanolaminate

Amorphous $Cu_{50}Zr_{50}$/nanocrystalline (nc) Cu nanolaminates were deposited on Si(100) wafers by direct current magnetron sputtering. The thicknesses of the CuZr (amorphous) and nc Cu layers are 100 nm and 10 nm, respectively. The total stacked thickness of the CuZr/nc Cu nanolaminates is 1200 nm with an amorphous CuZr topmost layer. To study the local atomic arrangement dominated-deformation, nano-pillars with an initial diameter of 630 nm were fabricated, using a dual-beam focused ion beam (FIB) and tested with a Hysitron Ti 950 triboindenter with a flat punch. The SEM images of these nanopillars before and after compression are shown in Fig. 1(a). Those surface markings/cracks hint that shear-banding is caused by the local non-Newtonian flow. It is noted that the formation and evolution of shear bands control the yielding and plasticity of almost all MGs at room temperature. In most cases, the formation of dominant shear bands quickly leads to failure [32]. These results show that the presence of a ductile nanocrystalline phase in the nanolaminates can slow down the speed of shear-band propagation and prevent catastrophic shear banding. According to the STZ concept, a group of atoms in the STZ can endure a much larger atomic displacement than that in the surrounding matrix in a shear transformation, contributing to an overall macroscopic strain.

The stress-strain curves of the samples tested with a strain rate of 1×10^{-3} s^{-1} are shown in Fig. 1(b), indicating a maximum strength of ~ 1.4 GPa. These classical Type-C [1] serration steps in the stress-strain curves, which are often observed at low strain rates and known as one type of Portevin-Le-Chatelier (PLC) effect, exhibites a strong strain-hardening effect in the 10-nm CuZr/Cu nanolaminates with the significantly-enhanced strength, supporting the hypothesis of "smaller is stronger" [13]. Similarly, it has been reported that the maximum strength of Cu/$Cu_{60}Zr_{40}$ A/C NLs increases from ~1.7 ± 0.05 GPa to ~2.3 ± 0.1 GPa, as the thickness of the A/C NL decreases from 100 to 20 nm [13].

Moreover, the thinner $Cu_{60}Zr_{40}$/Cu A/nC NLs with a ratio of 5/35 (a 5-nm-thick metallic glass and 35-nm-thick nanocrystalline in sequence) and equal layer thicknesses varying from 20 to 100 nm exhibit more pronounced softening behavior due to a greater number of A/C interfaces acting as dislocation sinks [13,33]. This mechanical heterogeneity (i.e., serrations) is believed to be connected to the intrinsic atomic packing described in several prevailing models, including the free volume, STZ, liquid-like zone, flow unit, and flexibility volume [3,7,34]. These models are usually based on the assumption of the existence of a structural defect or inefficient local atomic packing in the MG, which leads to the formation of heterogeneously-dense and loose regions [3,34], the same as the aforementioned soft spots.

Fig. 2 displays the low and high resolution TEM images of the A/C nanolaminates with the alternating CuZr and Cu layers before and after the micro-compression test. After micro-compression, the ordered "clusters" (to be identified in detail) form in the amorphous CuZr layers, both in the CuZr matrix and along the A/C interface, presenting a local disorder-order transformation and contributing to the serration behavior. Moreover, compositional mapping shows that there are many regions forming short-range ordered fine structures, which are enriched by either Cu or Zr, resulting in a large lattice distortion caused by the difference in relative atomic

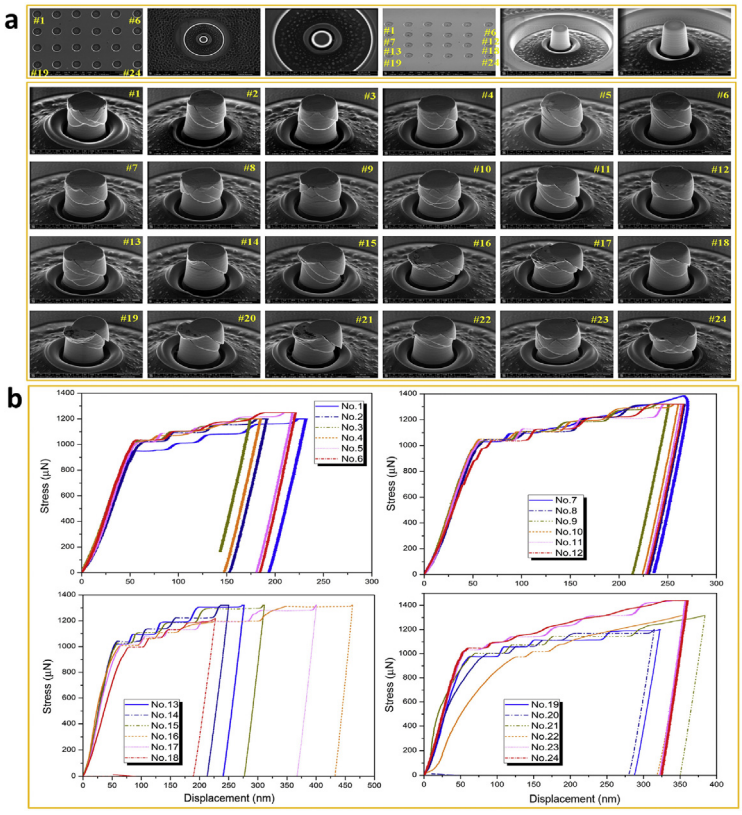

Fig. 1. High-throughput compression tests of CuZr/Cu nanopillars with a ~600 nm diameter: (a) SEM images of nanopillars with different views; (b) stress-displacement curves of the tested samples at a strain rate of 1×10^{-3} s^{-1}. The top and side views of the nanopillars before compression are presented in the first row of (a) while the side views of nanopillars after compression are listed in the other rows.

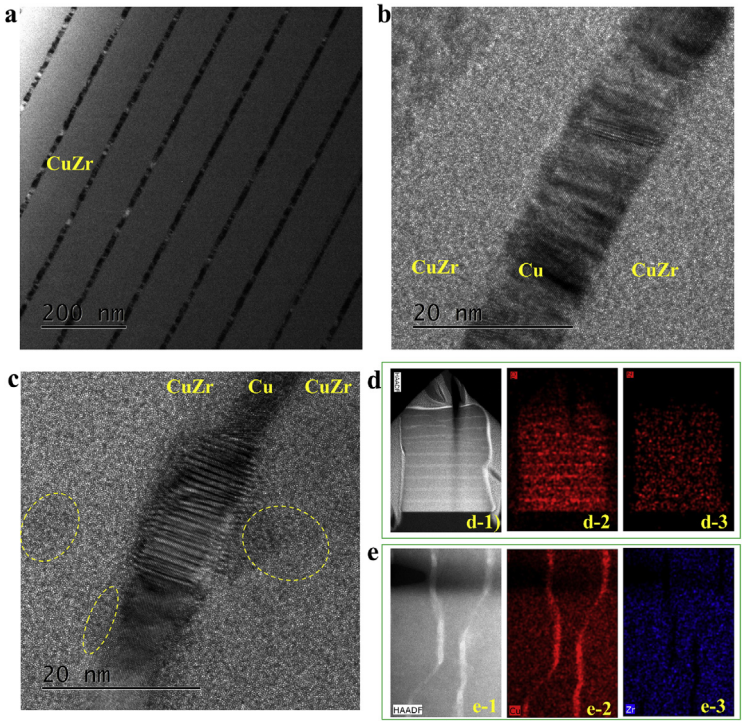

Fig. 2. Microstructures of the CuZr/Cu nanolaminates before and after micro-compression: (a, b) TEM images of the multilayers of the as-fabricated CuZr/Cu nanolaminates; (c-e) High-resolution TEM images and composition mapping of the sample after micro-compression. The CuZr/Cu NLs consist of 100-nm amorphous CuZr and 10-nm nanocrystalline Cu layers. The ellipses in **c** highlight the ordering clusters in the amorphous CuZr layer.

sizes. It is known that configurational transformations (local structure variations/relaxations) [34–36] represent transitions between various configurational states, such as those corresponding to atom interactions/rearrangements or transitions between different electronic states/microstates, phase transformations between aggregate states, or groups of processes with configurational transitions. The densely-packed short-range ordered structures, together with the loosely-packed weak spots of various geometrical configurations, are universal structural characteristics of MGs [2,3]. Therefore, with the use and guidance of electron redistribution functions, the contributions of these configurational transitions to the elastic and plastic properties can be captured [3]. The introduction of softness, which is a particle-based quantity, depending only on the local structural environment and a weighted integral over the local pair correlation function [37], provides a new way to link the structure-property relationships via the atomic rearrangements – the so-called configurational transitions. To understand the underlying transformation mechanism, more detailed information of the simulations on the deformation of CuZr/Cu A/C NLs are discussed as follows.

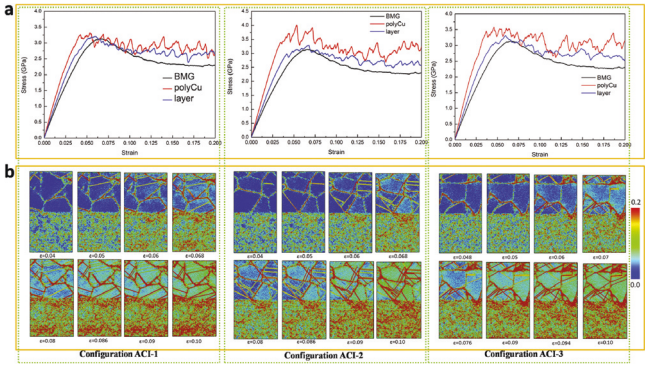

Fig. 3. Configurational transformation dominated serrations of CuZr/Cu NLs under strain rate of 1×10^8 s^{-1}: (a) hydrostatic stress versus axial strain along the *z* direction of the polycrystalline Cu, amorphous CuZr, and the CuZr/Cu NLs; (b) Von-Mises shear-strain distributions for the CuZr/Cu NLs calculated by MD simulations. The three independent structures/supercells shown are different in their Cu polycrystalline structures since only one amorphous CuZr layer from *ab initio* MD calculations are utilized here. The BGR gradient colors in (b) correspond to various levels of Von-Mises shear strains.

3.2. Atomic and electronic features of CuZr/Cu A/nC NL

The atomic structures of the CuZr/Cu A/nC NL, consisting of the Cu nano-polycrystals and amorphous CuZr, are constructed by Poisson Voronoi tessellations and *ab initio* molecular-dynamic calculations (AIMD), respectively. Three independent amorphous CuZr structures making up the enlarged supercells with 200 atoms were individually computed using AIMD at 1800 K, 1600 K and 1400 K (see Fig. S1 in Supporting Information). Firstly, the pair-correlation functions of the amorphous CuZr are compared with the available high-energy X-ray diffraction (XRD) and neutron diffraction (ND) measurements, showing a good agreement between the experiments and predictions (see Fig. S2). Secondly, the bonding structures of the single-crystal Cu and amorphous CuZr A/nC NLs are characterized by the bonding charge density ($\Delta\rho$) [3,38–41], which provides an electronic and atomic sight into the physical nature of the weak spots in CuZr and confirms their spatial distinction. It is understood that the higher the density of $\Delta\rho$ indicates the stronger the chemical bond strength [3]. Due to differences in atomic sizes and valence electrons between Zr and Cu, weak spots enriched of Cu are presented as those loosely-bonded and voids with few bonding charge densities, revealing the physical features of weak spots in the amorphous CuZr (see Fig. S3). Because the CuZr bond is much stronger than that of CuCu, this feature results in the initial yielding of the soft Cu layers, followed by the deformation of the CuZr layer in the A/C NLs.

3.3. Serration behavior of CuZr/Cu A/nC NLs

In order to reveal the physical nature of the serration behavior of the CuZr/Cu A/nC NLs, the configuration-mediated stress fluctuations in the stress-strain curves have been predicted by the MD calculation, shown in Fig. 3. The fluctuations of the stress-strain curves around 2.5 GPa indicate multiple configuration transitions that amplify the shear-relaxation process, which have been reported in both CuZr MGs and CuZr/Cu A/C NLs [42–45]. The Von-Mises shear-strain distribution is utilized to show and differentiate the elastic and plastic deformations, of which, the latter is also considered as an indicator for characterizing the STZs or large-scale shear bands [7,42,44]. The responses of the nanocrystalline Cu, amorphous CuZr, and the amorphous/crystalline interface (ACI) to the plastic deformation are now discussed individually. More information can be found in Figs. S5 and S6 and Movies S1 of the Supporting Information. Within the nanocrystalline Cu, one and two layers of atoms with large Von-Mises shear strains form transgranular twin boundaries and deformation faults, respectively. It has been shown that an edge dislocation in the FCC Cu can dissociate into a leading and a trailing Shockley partial linked by a stacking fault, with its Burgers vector reducing from a value of b = 2.56 Å for the perfect case of {111}<110> to a value of b = 1.48 Å for the partial {111}<112> [42]. Due to the plastic anisotropy that has been found experimentally and theoretically in the nano-twined Cu, there are three entirely different deformation behaviors that correspond to the external loading directions with respect to twin boundaries (TBs): (i) dislocation glide in between the twins; (ii) dislocation transfer across TBs; and (iii) dislocation-mediated TB migration [46,47]. Similarly, partial/fully developed screw dislocations have been observed in the singlecrystal Cu layer of the $Cu/Cu_{46}Zr_{54}$ A/C NLs, with the dislocations forming at the ACI [42]. Therefore, it is expected that the nanocrystalline Cu would exhibit a strain-hardening effect by the multiplications of nano-twins, stacking faults, and dislocations, which occur in the early stage of deformation; see the stress-strain curves in Fig. 3(a) and the corresponding structure evolution of the Cu layer in Fig. 3(b). Moreover, a strong interaction between the dislocations/stacking faults and the ACI has been observed, resulting in a large local Von-Mises shear strain even at low global strains, highlighted by the ellipses in Fig. 3(b). It has been reported that the nanocrystalline Cu has the intrinsic plasticity and the role of the ACI is for the load transfer [48]. For example, the 1/6 < 112> Shockley partial dislocation could nucleate at the ACI, between the nanocrystalline Cu and the amorphous $Cu_{50}Zr_{50}$ layers, which then can be transmitted across the Cu layer along the {111} plane, followed by the formation of a stacking fault [44]. Additionally, there are two other significant roles for the ACI, which leads to a work-softening effect, (i) attracting/annihilating the dislocations, thereby sharply reducing their density; and (ii) enhancing the local strain along the ACI and activating STZs in a correlated fashion near the intersection line between the dislocation slip plane and the ACIs without the need for significant atomic rearrangements in the local amorphous matrix [33,42,49].

As for the amorphous CuZr layer, even within the elastic region, it can be seen that a few weak spots endure a higher shear strain than other parts of the amorphous CuZr. With increasing the strain, groups of weak spots accumulate and form larger regions (or STZs) facilitating further deformations and flows, and eventually reach the threshold that triggers self-sustaining shear banding, the result of which is the homogeneous flow dynamics that produces a smooth stress-strain curve. It is the interactions between the various flow units of weak spots, GUMs, or STZs, etc. that result

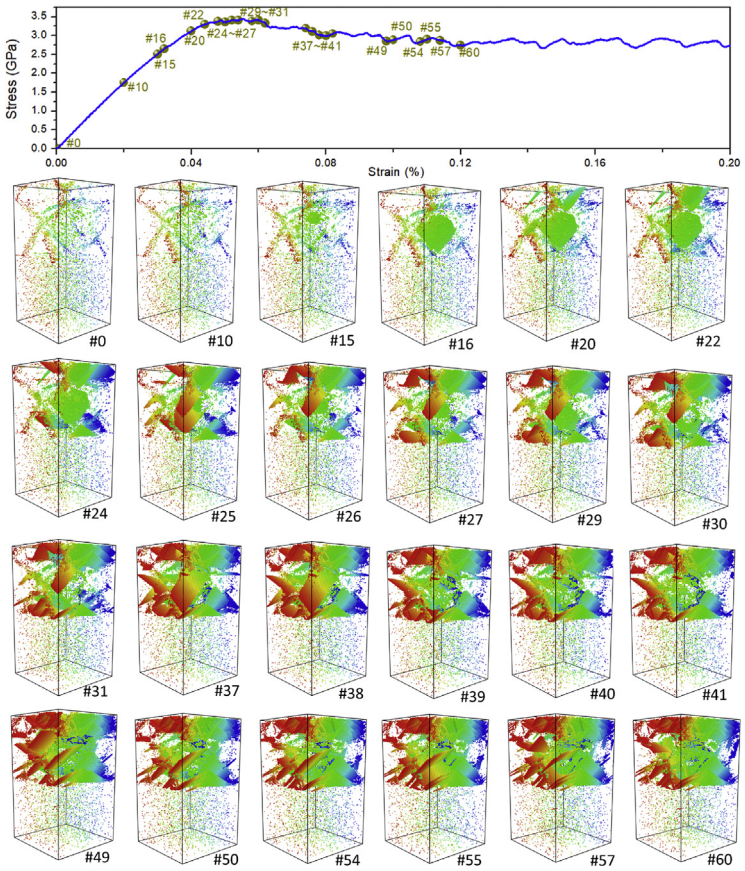

Fig. 4. Snapshots of configurations corresponding to the stress-strain curve of the CuZr/Cu NLs under a strain rate of 1×10^8 s^{-1}. The HCP-type structures that are produced to create a deformation fault (2 layers combined together) and twin boundaries (the isolated single layer), BCC-type ordering at grain boundaries of Cu, and amorphous CuZr, and atoms constructing the Voronoi polyhedra of CuZr are selected through deleting the FCC matrix of the polycrystalline Cu and disordered structures of the amorphous CuZr. The BGR gradient colors are utilized to identify the atomic spatial coordinates.

in the macroscopically observed plastic flow in the amorphous CuZr layer. It is also found that there are ongoing disorder-order transformations, yielding a number of BCC-type nanoprecipitates in the amorphous matrix, which are identified by the regions having large Von-Mises shear strains. The formation of BCC-type nanoprecipitates is closely linked to the localized shear flow, i.e., STZ-mediated activities. This feature not only validates the classical DID phenomena, but also is consistent with the previous observations of the B2-CuZr [12], the orthorhombic $Cu_{10}Zr_7$ [49], or the other nanoprecipitates [21] that form in the amorphous CuZr during deformation. Therefore, the combined effects of the dislocation plasticity, STZ activities, and DID induced precipitation hardening determine the aforementioned and observed Type C serration behavior of the CuZr/Cu A/C NL.

4. Discussion

4.1. Effect of structural relaxation on deformation

According to the theoretical models of the atomic structures of MGs, weak spots are always composed of the loosely-bound atoms associated with various short- or medium-range ordered regions, which can cause the sudden burst of atomic motion and slip avalanche, followed by the formation of new types of bonds/clusters during deformation [3]. Recent studies have revealed that the energy barrier for the β relaxation (i.e., early stage) is very close to that for shear transformation in an isolated/individual STZ, suggesting that MGs with the pronounced β-relaxation at relatively low temperatures might be macroscopically ductile [22,50]. Such a plastic-flow dilatation in the localized region would rearrange the topology of local atoms, alter their short range order [21], and thus result in configurational transitions and thus the formation of novel weak spots. Once initiated, a slipping weak spot can also trigger other weak spots to slip, and create what is referred to as a slip avalanche, and result in structural rejuvenation [3]. Weak spots, associated with configurational transitions and the strain response of softening beyond yielding, have been considered as the structural signatures of the amorphous alloy or MG deformation behavior.

Although great efforts have been devoted to nanolaminates with elastic/plastic or stable/unstable interfaces under extreme conditions, the fundamental principles that account for their deformation behavior are still not fully understood [19,23,44,49,51,52]. In particular, it is unclear what the role of these crystalline phases in A/C nanolaminates during shear band propagation is [21,42]. Since the deformation of A/C nanolaminates is sensitive to many factors, including the lattice mismatch, crystal defects, impurities, and reactions at the A/C interface, it remains very challenging to understand their deformation mechanisms solely via a strictly-experimental approach [44]. However, integrated with the experiments, our molecular-modeling framework developed herein is able to capture the details of deformation at the atomic-scale to elucidate and understand the mechanisms for Type-C serrations within the CuZr/Cu A/C nanolaminates presented in Fig. 1(b). Fig. 4 shows the snapshots of configurations at the different stages of loading of the stress-strain curves under a strain rate of 1×10^8 s^{-1}. To highlight the configurational transitions of the FCC Cu and amorphous CuZr, the FCC matrix of the Cu polycrystals and the disordered structures of the amorphous CuZr are intentionally deleted in Fig. 4. The accumulation of the HCP-type structures for deformation faults (2 layers combined together) and twin boundaries

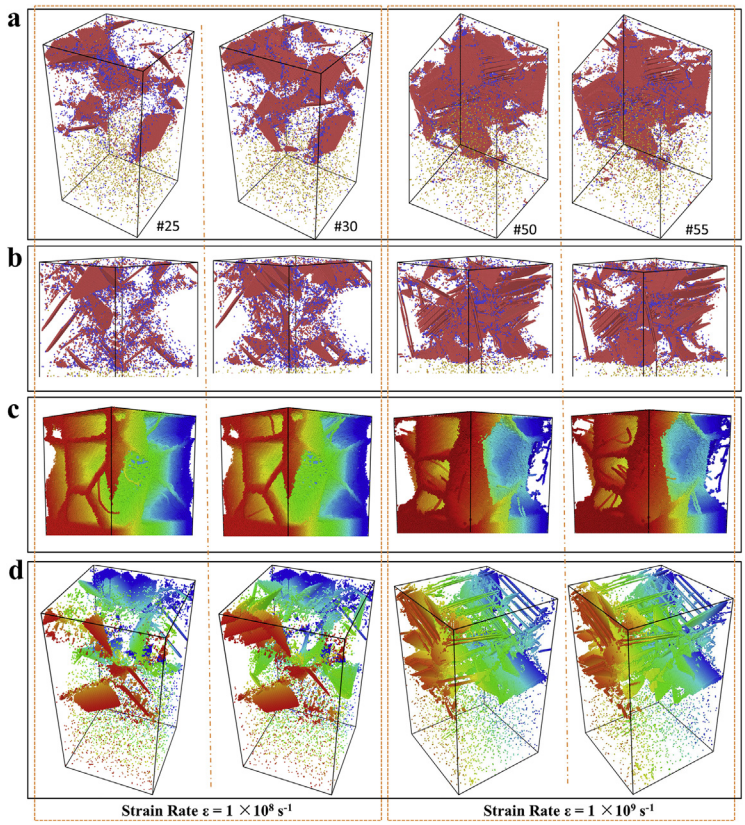

Fig. 5. Various views of the configurational transformations of the CuZr/Cu NLs under strain rates of 1×10^8 s^{-1} and 1×10^9 s^{-1}: (a) the resultant HCP-type structure for deformation faults (2 layers combined together) and twin boundaries (the isolated single layer) in red, BCC-type ordering at Cu grain boundaries and the amorphous CuZr in blue, and atoms constructing the Voronoi polyhedra of CuZr in green; (b) an enlarged region of the nanocrystalline Cu shown in (a); (c) the evolution of the disordered structures in the nanocrystalline Cu, trailing the edge of the stacking faults and the (partial) dislocations shown with the BGR gradient; (d) BGR view of the HCP and BCC regions, and the Voronoi polyhedra discussed in (a).

(an isolated single layer) contribute to the strain-hardening effect. There is also a twinning-detwinning behavior of Cu (see Movie S1 for more information), resulting in another type of the configuration transition and a corresponding stress fluctuation. The BCC-type ordering occurs at grain boundaries of the Cu and in the amorphous CuZr (Figs. S7 and S8). The presence within the latter validates the classical DID behavior observed in MGs. The disordered structures including the amorphous CuZr, the atoms at grain boundaries, and dislocations (or the edge of stacking faults), are shown in Fig. S9. It can be clearly seen that both the grain boundaries and the ACI act as the source and sink for dislocations, thus influencing the movement of dislocations. As shown in Fig. 4, while the Voronoi polyhedra could be considered as the backbones of the amorphous CuZr layer [15], the DID-aided superior deformability via "externally-supplied" dislocations-stimulated-STZs around the GUM occur. Similarly, under the shock loading conditions, it was reported that the single crystal Cu layers of the $Cu_{63}Zr_{37}$/Cu A/C NLs experience a FCC-BCC transformation while the <0446> and <0447> Voronoi Polyhedra form in the CuZr [16]. The grain boundaries act as the nucleation site of BCC phase during the high-velocity shock propagation [16]. It is revealed that the ACIs always endure the maximum slip strain, which indicate that plasticity carriers accumulate at the interface and are absorbed there [17]. In this manner, the serration behavior of the CuZr/Cu A/C nanolaminates originates from the combined effect of the multiplication of the initial dislocations, formation of dense dislocation networks after yielding, weak spots related configurational transitions, STZ activities, and DID behaviors. This improved understanding paves a path on the development of self-toughening MG-based composites and A/C nanolaminates [13,19].

4.2. Effect of strain rate on deformation

Various serration behaviors are sensitive to the loading conditions, loading rate, sample size, microstate/microstructure of the materials, and so on [1,21,44]. Therefore, it is necessary to determine effect of the strain rate on the deformation mechanisms of the CuZr/Cu A/C nanolaminates. To this end, various types of configurational transformations were selected, as exhibited in Fig. 5. In general, the serration types are disparate at different strain rates [1], but this trendis not clearly observed due to the high strain rates applied in the MD simulations. However, there is a similar structural evolution ongoing during the deformation. In particular, the HCP-type structures of the deformation faults and twin boundaries are highlighted in red, BCC-type ordering at grain boundaries of the Cu and the amorphous CuZr in blue, and atoms in the Voronoi polyhedra of CuZr in green, as shown in Fig. 5(a) and (b). The evolution of the disordered structures in the crystalline Cu layer, is the tail edge of the stacking faults and the (partial) dislocations, characterized with a Blue-Green-Red (BGR) gradient in Fig. 5(c). Finally, the networks constructed from these ordered structures of HCP, BCC, and the Voronoi polyhedra are identified by their positions in BGR, as shown in Fig. 5(d). The parallel patterns formed by the HCP layers indicate that only a single slip system with a slip plane inclined to the grain boundaries is active, which is similar to the observations in the nanotwinned Cu [53]. It should be noticed that the BCC-type ordering in the amorphous CuZr is mainly caused by the atomic rearrangement [12,13], which is the so-called configurational transformation, instead of the adiabatic heat-affected zone despite the utilized strain rates being very high. This feature is due to the fact that (i) there are so many weak spots

in the initial amorphous CuZr, as shown in Fig. S3, which could lead to slip avalanche or structural rejuvenation [3]; and (ii) it has been proven that the shearing of the amorphous CuZr leads to atomic displacements, which result directly in crystallization [12] and demonstrate the DID behavior [13]. The ability to study the atomic structures and configurational transformations within the CuZr/Cu A/C nanolaminates is very useful for understanding the physical nature of the underlying deformation mechanisms in such composite structures, and the results from our combined molecular-modeling effort thus provide the supporting guidance for the design of high-performance nanolaminates.

5. Conclusion

In summary, the present work revealed the configurational-transition-dominated Type-C serration behavior of CuZr/Cu A/nC nanolaminates. In an atomistic view, the serrations are constituted of the multiplication of the initial dislocations forming dense dislocation networks within the nanocrystalline layer, the formation and activity of weak-spots-related configurational transitions and STZs, as well as DID behavior characterized by the formation of BCC-type nanoprecipitates in the amorphous matrix. With increasing deformation and strain, the creation of weak spots in the amorphous layer, preceded by dislocation mediated twinning in the nanocrystalline layer, forms a shear band leading to a drop in the stress, creating the appearance of the serrated flow. Specifically, it is found that the serrated flow of nanolaminates is a result of the combined effects of the formation of HCP-type stacking faults and twins inside the FCC Cu grains, lowering the load-bearing capacity of these regions, the BCC-type ordering at Cu grain boundaries, and the ordering in the amorphous CuZr. These findings from the nanoscale experiments and molecular simulations of atomic structures and configurational transformation of the CuZr/Cu A/C NLs provide a theoretical basis for the continued development of self-toughening MG-based composite structures.

Acknowledgements

This work was financially supported by the National Natural Science Foundation of China (Nos. 51690163 and 51601147), the Science Challenge Project (No. TZZT2019-D1.5), the Ministry of Science and Technology of China (No. 2017YFA0700700), the United States National Science Foundation (Nos. DMR-1006557, 1611180, and 1809640), and the Fundamental Research Funds for the Central Universities in China (No. G2016KY0302). W.Y. Wang and B. Gan would like to thank Dr. Wei Guo for fruitful discussions. First-principles calculations were carried out on the clusters at Northwestern Polytechnical University. Calculations were also carried out on the CyberStar cluster funded by NSF through grant No. OCI-0821527 and the XSEDE clusters supported by NSF through Grant No. ACI-1053575.

Appendix A. Supplementary data

Supplementary material related to this article can be found, in the online version, at doi:https://doi.org/10.1016/j.jmst.2020.04.024.

References

[1] Y. Zhang, J.P. Liu, S.Y. Chen, X. Xie, P.K. Liaw, K.A. Dahmen, J.W. Qiao, Y.L. Wang, Prog. Mater. Sci. 90 (2017) 358–460.
[2] J. Ding, S. Patinet, M.L. Falk, Y. Cheng, E. Ma, Proc. Natl. Acad. Sci. U. S. A. 111 (2014) 14052–14056.
[3] W.Y. Wang, S.L. Shang, Y. Wang, F. Han, K.A. Darling, Y. Wu, X. Xie, O.N. Senkov, J. Li, X.D. Hui, K.A. Dahmen, P.K. Liaw, L.J. Kecskes, Z.K. Liu, NPJ Comput. Mater. 3 (2017) 23.
[4] A.M. Beese, Z. Wang, A.D. Stoica, D. Ma, Nat. Commun. 9 (2018) 2083.
[5] J.J. Li, J.W. Qiao, K.A. Dahmen, W.M. Yang, B.L. Shen, M.W. Chen, J. Iron Steel Res. Int. 24 (2017) 366–371.
[6] J.J. Li, J.F. Fan, Z. Wang, Y.C. Wu, K.A. Dahmen, J.W. Qiao,Intermetallics 116 (2020), 106637.
[7] N. Wang, J. Ding, F. Yan, M. Asta, R.O. Ritchie, L. Li, NPJ Comput. Mater. 4 (2018) 19.
[8] A. Widmer-Cooper, H. Perry, P. Harrowell, D.R. Reichman, Nat. Phys. 4 (2008) 711–715.
[9] M. Chen, A. Inoue, W. Zhang, T. Sakurai,Phys. Rev. Lett. 96 (2006), 245502.
[10] J.J. Kim, Y. Choi, S. Suresh, A.S. Argon, Science 295 (2002) 654–657.
[11] Y. Wang, J. Zhang, K. Wu, G. Liu, D. Kiener, J. Sun, Mater. Res. Lett. 6 (2018) 22–28.
[12] S. Pauly, S. Gorantla, G. Wang, U. Kuhn, J. Eckert, Nat. Mater. 9 (2010) 473–477.
[13] J.Y. Zhang, G. Liu, J. Sun, Sci. Rep. 3 (2013) 2324.
[14] M. Mosayebi, P. Ilg, A. Widmer-Cooper, E. Del Gado,Phys. Rev. Lett. 112 (2014), 105503.
[15] E. Ma, J. Ding, Mater. Today 19 (2016) 568–579.
[16] K.V. Reddy, C. Deng, S. Pal, Acta Mater. 164 (2019) 347–361.
[17] M.Y. Tong, C.K.C. Lieou, I.J. Beyerlein,Phys. Rev. Mater. 3 (2019), 073602.
[18] Y.W. Luan, C.H. Li, X.J. Han, J.G. Li, Mol. Simul. 43 (2017) 1116–1124.
[19] W. Guo, E.A. Jaegle, P.P. Choi, J. Yao, A. Kostka, J.M. Schneider, D. Raabe,Phys. Rev. Lett. 113 (2014), 035501.
[20] Y.Q. Wang, J.Y. Zhang, X.Q. Liang, K. Wu, G. Liu, J. Sun, Acta Mater. 95 (2015) 132–144.
[21] W. Guo, B. Gan, J.M. Molina-Aldareguia, J.D. Poplawsky, D. Raabe, Scr. Mater. 110 (2016) 28–32.
[22] Y.Q. Cheng, E. Ma, Prog. Mater. Sci. 56 (2011) 379–473.
[23] X.L. Ma, C.X. Huang, W.Z. Xu, H. Zhou, X.L. Wu, Y.T. Zhu, Scr. Mater. 103 (2015) 57–60.
[24] J. Qiao, H. Jia, P.K. Liaw, Mater. Sci. Eng. R 100 (2016) 1–69.
[25] P.A. Hirel, Comput. Phys. Commun. 197 (2015) 212–219.
[26] S. Nose, J. Chem. Phys. 81 (1984) 511–519.
[27] W.G. Hoover, Phys. Rev. A 34 (1986) 2499–2500.
[28] S. Plimpton, J. Comput. Phys. 117 (1995) 1–19.
[29] M.I. Mendelev, M.J. Kramer, R.T. Ott, D.J. Sordelet, D. Yagodin, P. Popel, Philos. Mag. 89 (2009) 967–987.
[30] A. Stukowski,Model. Simul. Mater. Sci. 20 (2012), 045021.
[31] F. Shimizu, S. Ogata, J. Li, Mater. Trans. 48 (2007) 2923–2927.
[32] A.L. Greer, Y.Q. Cheng, E. Ma, Mater. Sci. Eng. R 74 (2013) 71–132.
[33] Y. Wang, J. Li, A.V. Hamza, T.W. Jr Barbee, Proc. Natl. Acad. Sci. U. S. A. 104 (2007) 11155–11160.
[34] F. Zhu, A. Hirata, P. Liu, S. Song, Y. Tian, J. Han, T. Fujita, M. Chen,Phys. Rev. Lett. 119 (2017), 215501.
[35] A. Pasturel, N. Jakse, NPJ Comput. Mater. 3 (2017) 33.
[36] R.S. Berry, B.M. Smirnov, Phys. Rep. 527 (2013) 205–250.
[37] E.D. Cubuk, R.J.S. Ivancic, S.S. Schoenholz, D.J. Strickland, A. Basu, Z.S. Davidson, J. Fontaine, J.L. Hor, Y.R. Huang, Y. Jiang, N.C. Keim, K.D. Koshigan, J.A. Lefever, T. Liu, X.G. Ma, D.J. Magagnosc, E. Morrow, C.P. Ortiz, J.M. Rieser, A. Shavit, T. Still, Y. Xu, Y. Zhang, K.N. Nordstrom, P.E. Arratia, R.W. Carpick, D.J. Durian, Z. Fakhraai, D.J. Jerolmack, D. Lee, J. Li, R. Riggleman, K.T. Turner, A.G. Yodh, D.S. Gianola, A.J. Liu, Science 358 (2017) 1033–1037.
[38] P.N.H. Nakashima, A.E. Smith, J. Etheridge, B.C. Muddle, Science 331 (2011) 1583–1586.
[39] Y. Wang, W.Y. Wang, L.Q. Chen, Z.K. Liu, J. Comput. Chem. 36 (2015) 1008–1014.
[40] W.Y. Wang, S.L. Shang, Y. Wang, K.A. Darling, S.N. Mathaudhu, X. Hui, Z.K. Liu, Acta Mater. 97 (2015) 75–85.
[41] W.Y. Wang, B. Tang, S.L. Shang, J. Wang, S. Li, Y. Wang, J. Zhu, S. Wei, J. Wang, K.A. Darling, S.N. Mathaudhu, Y. Wang, Y. Ren, X.D. Hui, L.J. Kecskes, J. Li, Z.K. Liu, Acta Mater. 170 (2019) 231–239.
[42] B. Arman, C. Brandl, S.N. Luo, T.C. Germann, A. Misra, T. Cagin,J. Appl. Phys. 110 (2011), 043539.
[43] Y. Cui, Y. Shibutani, S. Li, P. Huang, F. Wang, J. Alloys Compd. 693 (2017) 285–290.
[44] H.Y. Song, J.J. Xu, Y.G. Zhang, S. Li, D.H. Wang, Y.L. Li, Mater. Des. 127 (2017) 173–182.
[45] E. Alishahi, C. Deng, Comput. Mater. Sci. 141 (2018) 375–387.
[46] L. Sun, X. He, J. Lu, NPJ Comput. Mater. 4 (2018) 6.
[47] Z.J. Wang, Q.J. Li, Y. Li, L.C. Huang, L. Lu, M. Dao, J. Li, E. Ma, S. Suresh, Z.W. Shan, Nat. Commun. 8 (2017) 1108.
[48] T.G. Nieh, J. Wadsworth, Intermetallics 16 (2008) 1156–1159.
[49] J.Y. Zhang, G. Liu, J. Sun, Acta Mater. 66 (2014) 22–31.
[50] H.B. Yu, W.H. Wang, K. Samwer, Mater. Today 16 (2013) 183–191.
[51] I.J. Beyerlein, J.R. Mayeur, S. Zheng, N.A. Mara, J. Wang, A. Misra, Proc. Natl. Acad. Sci. U. S. A. 111 (2014) 4386–4390.
[52] M.C. Liu, J.C. Huang, Y.T. Fong, S.P. Ju, X.H. Du, H.J. Pei, T.G. Nieh, Acta Mater. 61 (2013) 3304–3313.
[53] Q. Pan, H. Zhou, Q. Lu, H. Gao, L. Lu, Nature 551 (2017) 214.